

# Global dynamics of selective attention and its lapses in primary auditory cortex

Peter Lakatos<sup>1,2</sup>, Annamaria Barczak<sup>1</sup>, Samuel A Neymotin<sup>3,4</sup>, Tammy McGinnis<sup>1</sup>, Deborah Ross<sup>1</sup>, Daniel C Javitt<sup>1,5</sup> & Monica Noelle O'Connell<sup>1</sup>

Previous research demonstrated that while selectively attending to relevant aspects of the external world, the brain extracts pertinent information by aligning its neuronal oscillations to key time points of stimuli or their sampling by sensory organs. This alignment mechanism is termed oscillatory entrainment. We investigated the global, long-timescale dynamics of this mechanism in the primary auditory cortex of nonhuman primates, and hypothesized that lapses of entrainment would correspond to lapses of attention. By examining electrophysiological and behavioral measures, we observed that besides the lack of entrainment by external stimuli, attentional lapses were also characterized by high-amplitude alpha oscillations, with alpha frequency structuring of neuronal ensemble and single-unit operations. Entrainment and alpha-oscillation-dominated periods were strongly anticorrelated and fluctuated rhythmically at an ultra-slow rate. Our results indicate that these two distinct brain states represent externally versus internally oriented computational resources engaged by large-scale task-positive and task-negative functional networks.

One of the most prominent features of the brain is that it is never in a steady state; its operations perpetually fluctuate on multiple spatial and temporal scales. Often, these fluctuations are temporally regular and spectrally confined, and they can therefore be called oscillations. The most common types of neuronal oscillations occur on relatively small subsecond timescales, and reflect synchronous membrane potential fluctuations of a neuronal ensemble between depolarized and hyperpolarized states, which maintains ideal excitability<sup>1</sup>. Besides this thermostat-like function, the brain also evolved to make use of its neuronal oscillations in a number of other ways, including temporal coordination of neuronal operations via dynamic functional connectivity<sup>2,3</sup>, phase-coding of spatial aspects of the environment<sup>4,5</sup> and attentional selection<sup>6–8</sup>. While the subsecond timescale neuronal oscillations implementing these brain operations have been extensively studied and we have a reasonable amount of information on their dynamics and functional significance<sup>1</sup>, the neuronal underpinnings of long timescale fluctuations of brain states are not known, even though they are evident in neuroimaging studies<sup>9–11</sup>, electrophysiological data<sup>12–15</sup> and human behavioral measures<sup>16–18</sup>.

In the present study, our main goal was to define global, long-timescale fluctuations of the neuronal dynamics underlying attention and its lapses in auditory cortex. We explored these multisecond dynamics in the primary auditory cortex (A1) of nonhuman primates while they performed an intermodal selective attention task. Since the entrainment of neuronal oscillations by attended stimulus streams is well characterized in artificial and natural selective attention conditions, especially in primary sensory cortices<sup>7,19–21</sup>, we hypothesized that we

could use entrainment as an electrophysiological marker of attention and its fluctuations, allowing us to compare neuronal dynamics during precisely demarcated periods of selective attention and its lapses. To achieve this, we estimated the strength of entrainment in short-duration sliding timeframes throughout the performance of a continuous selective attention task. Using behavioral measures, we first verified that periods of entrainment versus lack of entrainment corresponded to periods of selective attention versus attentional lapses, respectively. Next, we compared neuronal ensemble dynamics during these two distinct brain states, and found that attentional lapses, besides showing the characteristic lack of oscillatory entrainment by external stimuli, were also characterized by increased alpha-frequency-band oscillatory activity across all cortical layers. Importantly, we found that entrainment-dominated versus alpha-dominated brain states fluctuated rhythmically in counterphase at a rate of approximately 0.06 Hz, independent of task structure, indicating that an internal mechanism is responsible for orchestrating global, long-timescale attentional dynamics. Analysis of neuronal ensemble and single-neuron dynamics during entrainment versus alpha-oscillation-governed brain states revealed noticeably different patterns of cross-frequency coupling, single-neuron activity and interlaminar coherence, likely supporting distinct externally versus internally oriented, or 'task positive' versus 'task negative' brain operations.

## RESULTS

We analyzed neuroelectric data recorded in 36 A1 sites of two macaque monkeys (20 sites in subject KI and 16 in subject AB). Neuronal activity

<sup>1</sup>Cognitive Neuroscience and Schizophrenia Program, Nathan Kline Institute, Orangeburg, New York, USA. <sup>2</sup>Department of Psychiatry, New York University School of Medicine, New York, New York, USA. <sup>3</sup>Department of Physiology & Pharmacology, SUNY Downstate Medical Center, Brooklyn, New York, USA. <sup>4</sup>Department of Neuroscience, Yale University School of Medicine, New Haven, Connecticut, USA. <sup>5</sup>Department of Psychiatry, Columbia University College of Physicians and Surgeons, New York, New York, USA. Correspondence should be addressed to P.L. ([plakatos@nki.rfmh.org](mailto:plakatos@nki.rfmh.org)).

Received 13 May; accepted 11 August; published online 12 September 2016; doi:10.1038/nn.4386

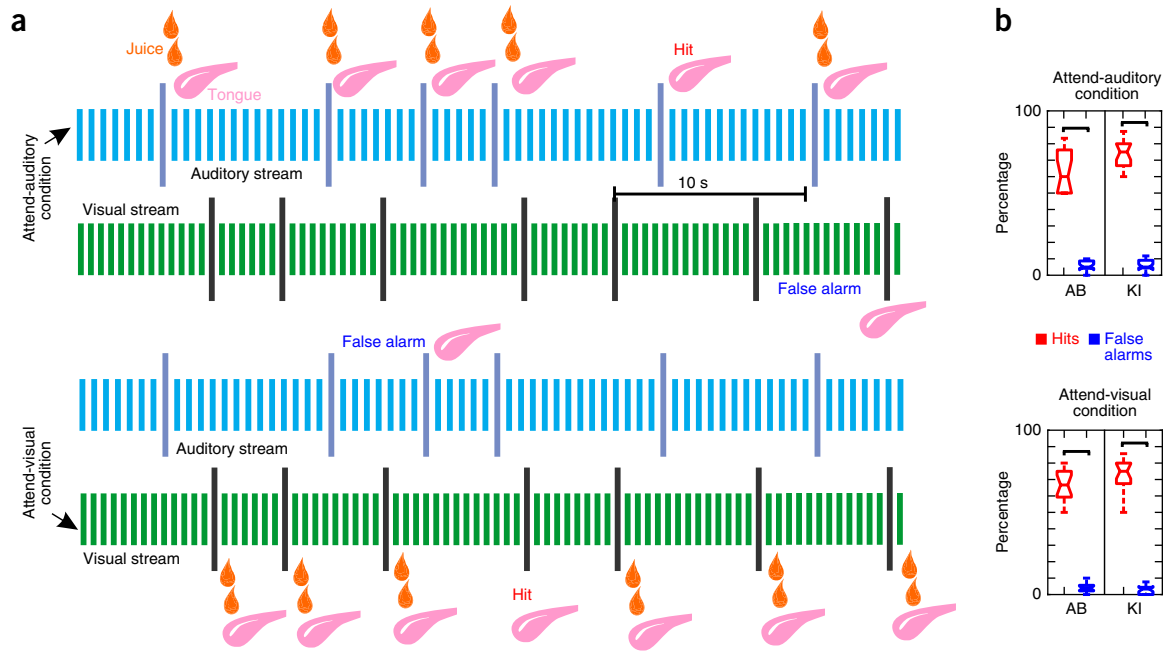


**Figure 1** Intermodal selective attention task. **(a)** All data presented were recorded while subjects were performing an intermodal selective attention task: they were cued to either detect deviant stimuli in the auditory (attend-auditory) or the visual (attend-visual) simultaneously presented stimulus sequences (streams). Visual and auditory stimuli were identical in the two different cue contexts. On 80% of the deviants of the cued modality, a juice reward (orange teardrops) was presented and the subject had to stick out her tongue in order to get it. Performance was monitored by detecting licking on juiceless deviants (hit). If subjects licked following a deviant in the noncued modality, we considered this a false alarm. Light blue and green lines represent auditory and visual standards, respectively, while dark blue and black lines represent auditory and visual deviants, respectively. **(b)** Both subjects' hit rates were significantly higher than their false alarm rates across experiments ( $n = 16$ ,  $P_{\text{auditory}} = 4.37 \times 10^{-4}$ ,  $P_{\text{visual}} = 4.37 \times 10^{-4}$  for subject AB and  $n = 20$ ,  $P_{\text{auditory}} = 8.83 \times 10^{-5}$ ,  $P_{\text{visual}} = 8.82 \times 10^{-5}$  for subject KI; Wilcoxon signed-rank tests). KI had a significantly higher hit rate (76% versus 64%) than AB across both attend-auditory and attend-visual trial blocks ( $n_{\text{AB}} = 16$ ,  $n_{\text{KI}} = 20$ , Wilcoxon rank-sum tests;  $P_{\text{auditory}} = 0.03$ ,  $P_{\text{visual}} = 0.02$ ). Mean false alarm rates were around 5% for both subjects, and did not differ significantly ( $n_{\text{AB}} = 16$ ,  $n_{\text{KI}} = 20$ , Wilcoxon rank-sum tests;  $P_{\text{auditory}} = 0.42$ ,  $P_{\text{visual}} = 0.49$ ). Boxplots have lines at lower quartile, median, and upper quartile values, while whiskers show the extent of the data.

was recorded with linear array multielectrodes, which spanned all cortical layers. In all experiments, data were obtained via simultaneous left and right hemisphere A1 recordings targeting regions tuned to similar frequencies. To minimize the effects of volume conduction, and to attempt to define local transmembrane currents, we calculated one-dimensional current source density (CSD) from the field potentials<sup>22</sup> and carried out our analyses on the CSD signals and on multi- and single-unit activities (MUA and SUA respectively).

During recordings, subjects performed a selective intermodal attention task (Fig. 1a). In separate blocks, the monkeys either had to attend to a rhythmic stream of auditory tone beeps and detect deviant tones (targets) that differed in their frequency, while ignoring the simultaneously presented visual stimulus stream (attend-auditory blocks); or they had to attend to rhythmically presented light flashes and detect deviant flashes (targets) that differed from standards either in color or intensity, while ignoring auditory stimuli (attend-visual blocks). Subjects were instructed to attend to a given modality by a cueing block that preceded selective attention trial blocks and consisted only of stimuli from the modality to be attended to. During the presentation of the selective attention trial blocks (lasting 187–239 s and containing 32–46 targets), 80% of targets were paired with a juice reward, which the subject could collect by sticking out her tongue. On 20% of targets, the juice reward was randomly omitted. These trials were used to monitor performance: a hit was detected if the subjects licked on the juiceless targets, while a false alarm was defined as a behavioral response to deviants of the noncued modality. Hit and false-alarm rates of the two subjects were significantly different in

both attend-auditory and attend-visual trial blocks (Fig. 1b), indicating that cueing had a strong effect on behavior.

### Ensemble oscillatory characteristics of attention and its lapses

As we outlined above, the first goal of our study was to generate a time-resolved measure for the strength of entrainment to determine whether it can be used to index attention. To do this, we first determined the cortical layers for each of our recording sites using CSD response profiles related to best-frequency (BF) tones (Fig. 2a) and selected the supragranular channel with the largest amplitude sink for intertrial coherence (ITC) analyses, since previous studies pinpoint this laminar location as the site of strongest oscillatory entrainment<sup>7,20,23</sup>. Albeit BF tone-related CSD profiles were used to determine laminar electrode locations, for our further analyses we selected artifact-free recordings during which non-BF tones constituted the auditory stream, with frequencies at least 2 octaves different from the BF of the recording site (Fig. 2a). The reason for this is that responses to non-BF tones are subthreshold in nature, without significant stimulus-related MUA or CSD amplitude increases (evoked responses) that could distort phase and ITC estimates<sup>20,24</sup>, which are used to index entrainment. Next, we extracted the phases of the supragranular delta oscillation that corresponded to the repetition rate of stimuli (auditory = 1.6 Hz and visual = 1.8 Hz) at stimulus onset in 5-s windows and calculated the ITC (Fig. 2b). The step size of the moving window was 1 s, resulting in a 1 Hz sampling rate. Significant ITC values related to stimuli from either modality indicated that delta oscillations in a given time window were 'locked to' or entrained by

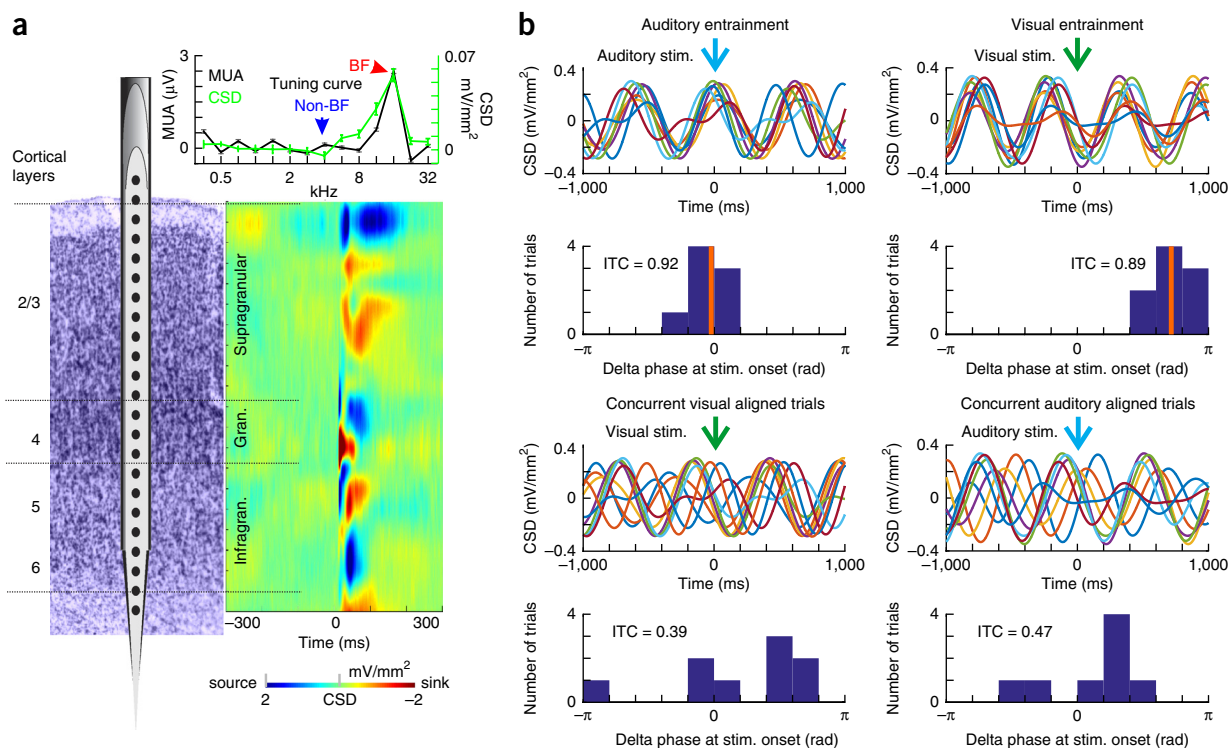


**Figure 2** Recording technique and ITC. **(a)** Left: schematic of the linear array multicontact electrode positioned in primary auditory cortex; right: color map showing a characteristic BF-tone-related laminar CSD response profile. Current sinks (net inward transmembrane current), red; current sources (net outward transmembrane current), blue. Lamina boundaries (horizontal lines) were determined based on functional criteria. Inset: the tuning curve for the representative A1 site derived from MUA (black) and CSD (green) response amplitudes to a range of different frequency pure tones. The arrowheads denote the BF (red) and a frequency 2 octaves away, designated as non-BF (blue). Gran., granular; infragran., infragranular. **(b)** An illustration of how our ITC measure, with a value range of 0 to 1, indexes phase alignment to stimuli in a given sensory stream. All traces in this figure panel show single trials of supragranular CSD, filtered in the delta frequency band (1–2.5 Hz). Top left: traces (top) depict 8 single trials aligned to the timing of auditory stimuli (stim., blue arrow) occurring within a 5-s time window. In this particular window, delta phases at stimulus onset are heavily biased (clustered in the histogram), resulting in significant delta ITC (Rayleigh test,  $n = 8$ ,  $P = 6.59 \times 10^{-6}$ ), and indicating entrainment. Bottom left: 9 single trials during the same 5-s period, but aligned to visual stimulus onset (green arrow). The histogram signifies a random delta-phase distribution with nonsignificant ITC (Rayleigh test,  $n = 9$ ,  $P = 0.24$ ). Right: both the single trial traces and the delta-phase distribution indicate entrainment to visual stimuli (Rayleigh test,  $n = 9$ ,  $P = 2.5 \times 10^{-5}$ ). In contrast, delta-band neuronal activity in the same time window is not aligned to the timing of the auditory stimuli that form the simultaneously presented auditory stream, resulting in nonsignificant ITC (Rayleigh test,  $n = 8$ ,  $P = 0.49$ ). The orange lines denote the mean phases of significantly biased phase distributions.

the stimuli, while nonsignificant ITC values signaled that the phase of oscillations was random at the time stimuli were presented due to a lack of oscillatory entrainment (**Fig. 2b**).

As **Figure 3a** illustrates, the moving ITC measure fluctuated strongly, both when calculated for auditory stimuli and for simultaneously presented visual stimuli, independent of whether the monkey was cued to attend to auditory or visual stimuli. Based on the significance of auditory- and visual-related moving ITC, four entrainment categories can be distinguished: (i) significant auditory-stimulus-related delta ITC (ITCa) indicating auditory entrainment, (ii) significant visual-stimulus-related delta ITC (ITCv) signaling visual entrainment, (iii) no significant ITC (noITC) and (iv) significant ITC related to both streams (ITCboth). As **Figure 3b** demonstrates, cueing, like behavior, also had a significant effect on entrainment. In attend-auditory trial blocks, auditory ITC periods occurred significantly more often than any other entrainment categories, and likewise visual ITC dominated in attend-visual trial blocks. The occurrence of periods marked by entrainment and lack of entrainment to the noncued modality did not differ significantly. Periods in which both auditory and visual ITC were significant (ITCboth) occurred significantly less often than any other entrainment category, and

sometimes not at all in a trial block (**Fig. 3a,b**). In line with previous studies<sup>20,23</sup>, these results indicate that, at least in A1, entrainment is exclusive: only one stimulus stream entrains oscillations at any given time. Therefore, we excluded time-windows when ITC was significant for both stimulus streams from further analyses.

To verify our initial hypothesis that oscillatory entrainment, measured as significant ITC, can be used as an indicator of selective attention, we examined the distribution of hits and false alarms during the different entrainment categories. As **Figure 3b** illustrates, nearly all hits occurred during periods of entrainment to the cued modality (82.9% in attend-auditory and 83.4% in attend-visual trial blocks), while nearly all false alarms occurred during periods of entrainment to the noncued modality (87.1% in attend-auditory and 76.1% in attend-visual trial blocks). This indicates that the modality of entrainment is indeed a good indicator for the modality the subjects are selectively attending to. Both entrainment and behavioral measures indicate that, while cueing successfully biased the monkey's attention toward the desired modality stimuli, at times the subjects were switching their attention to the noncued modality. During periods of no entrainment, the monkeys had significantly fewer hits compared to entrainment to the cued modality, and significantly

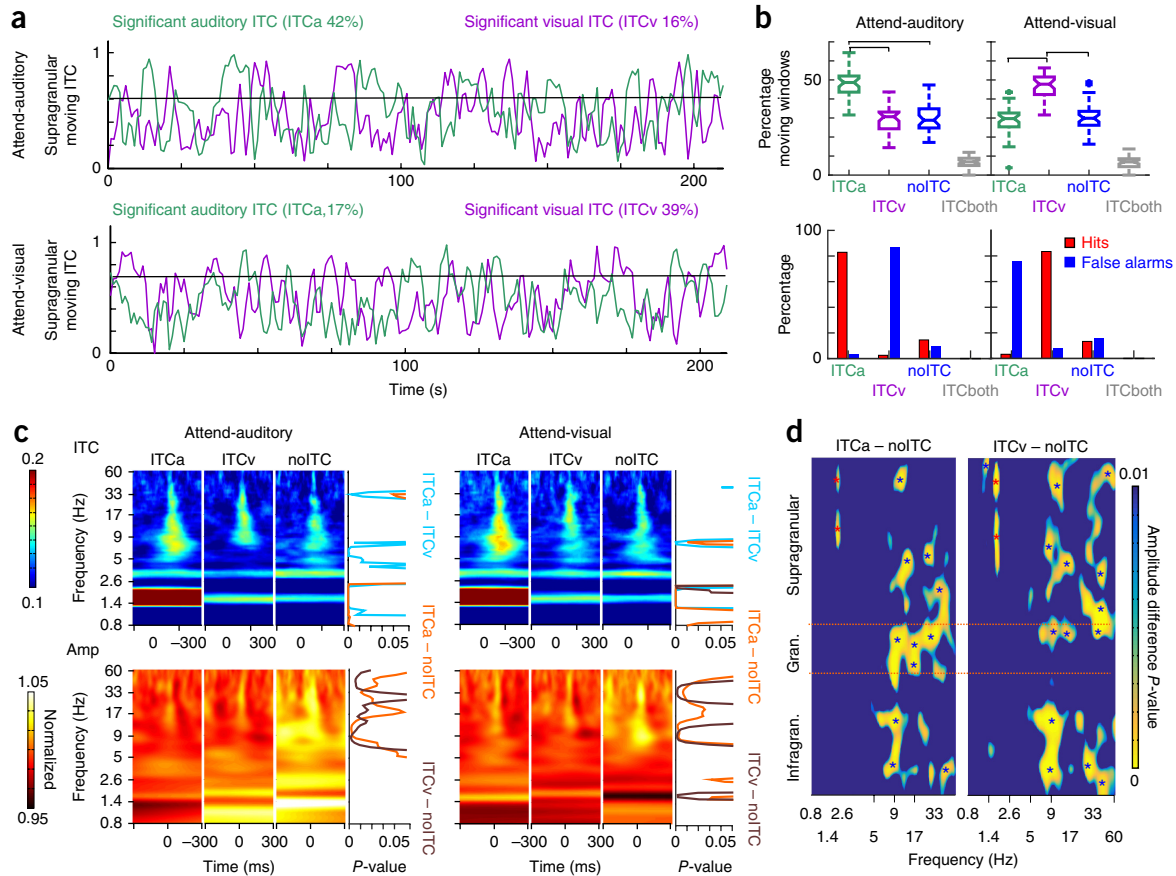


**Figure 3** Long-timescale dynamics of oscillatory entrainment during a continuous selective intermodal attention task. **(a)** Moving delta ITC values from a representative supragranular electrode site. Green traces were calculated using the timing of non-BF tones, while purple traces were calculated using the timing of light flashes in attend-auditory (top) and attend-visual (bottom) trial blocks. The black horizontal line denotes the level above which auditory moving ITC is significant. **(b)** Top: green and purple boxplots show the percentage of time windows with significant auditory (ITCa) and visual (ITCv) delta ITC respectively, during attend-auditory (left) versus attend-visual (right) trial blocks across all experiments ( $n = 36$ ). Blue and gray boxplots show the percentage of time windows with nonsignificant delta ITC related to any of the streams (noITC), and significant ITC related to both streams (ITCboth). Boxplots have lines at lower quartile, median, and upper quartile values, while whiskers show the extent of the data. Significant ITC, indicating entrainment, occurred significantly more related to cued modality streams ( $n = 36$ , Tukey's test, attend-auditory:  $P_{ITCa - ITCv} = 2.33 \times 10^{-6}$ ,  $P_{ITCa - noITC} = 3.67 \times 10^{-6}$ ,  $P_{ITCa - ITCboth} = 3.77 \times 10^{-9}$ ,  $P_{ITCv - noITC} = 0.99$ ,  $P_{ITCv - ITCboth} = 1.3 \times 10^{-7}$ ,  $P_{noITC - ITCboth} = 7.9 \times 10^{-8}$ ; attend-visual:  $P_{ITCa - ITCv} = 1.51 \times 10^{-6}$ ,  $P_{ITCa - noITC} = 0.97$ ,  $P_{ITCa - ITCboth} = 5.18 \times 10^{-7}$ ,  $P_{ITCv - noITC} = 1.32 \times 10^{-5}$ ,  $P_{ITCv - ITCboth} = 3.77 \times 10^{-9}$ ,  $P_{noITC - ITCboth} = 4.89 \times 10^{-8}$ ). Bottom: percentage of hits and false alarms during the same four time periods demarcated by differing ITCs (ITCa, ITCv, noITC and ITCboth). Hits during noITC occurred significantly less often than during entrainment by the cued modality stimuli ( $n = 36$ , Wilcoxon signed-rank test,  $P_{attend-auditory} = 1.8 \times 10^{-7}$ ,  $P_{attend-visual} = 1.4 \times 10^{-7}$ ), and false alarms occurred significantly less frequently than during entrainment by the noncued modality stimuli ( $P_{attend-auditory} = 7.8 \times 10^{-4}$ ,  $P_{attend-visual} = 3.5 \times 10^{-6}$ ). **(c)** Auditory non-BF stimulus related ITC (top) and amplitude (bottom) time-frequency plots averaged across attend-auditory (left) and attend-visual (right) trial blocks during ITCa, ITCv and noITC time periods. Right of the plots, traces show frequency-specific  $P$ -values (Wilcoxon signed-rank tests, corrected) derived from statistically comparing ITC and amplitude values amongst ITCa - ITCv (blue), ITCa - noITC (orange) and ITCv - noITC (brown) time periods. **(d)** Laminar profiles of frequency-specific, Bonferroni-corrected  $P$ -values derived from statistically comparing amplitudes between ITCa - noITC and ITCv - noITC time periods across all experiments ( $n = 36$ ) and cueing conditions ( $n = 36 \times 2 = 72$ , Wilcoxon signed-rank tests). Blue color,  $P > 0.01$ ; red stars,  $P < 0.001$ , indicating significantly larger amplitudes in ITCa or ITCv versus noITC conditions; blue stars indicate significantly larger amplitudes during noITC time periods. Gran., granular; Infragran., infragranular.

fewer false alarms compared to entrainment to the noncued modality streams (**Fig. 3b**), indicative of attentional lapses.

Taken together, these results provide solid support for our hypothesis that oscillatory entrainment can be used to index the modality and strength of selective attention and that differing entrainment patterns outline distinct brain states: one indicative of selective attention to the auditory stream (ITCa), one of selective attention to the visual stream (ITCv) and a third state of attentional lapse (noITC). To reveal mechanistic information, we investigated how neuronal oscillatory dynamics differ across these three attentional states. We started by comparing supragranular auditory-stimulus-related ITC and power spectra averaged across all layers (**Fig. 3c**). As expected,

and as **Figure 3c** illustrates, auditory-stimulus-related ITC is greater at certain frequencies during auditory entrainment, independent of cueing context. One of these frequencies is delta, since significant delta ITC was used to define auditory entrainment. Other frequencies correspond to theta and gamma oscillations, which have been shown to be dominant in the spectrum of ongoing supragranular neuronal ensemble activity<sup>24</sup>. This is also expected since the phase reset of ongoing oscillations, indexed by ITC, is a prerequisite for entrainment, and prior studies have found that phase reset in the theta and gamma frequency bands accompanies delta reset and entrainment<sup>24</sup>. A two-way ANOVA carried out on ITC values averaged within the different frequency bands in the 20–100 ms post-stimulus timeframe

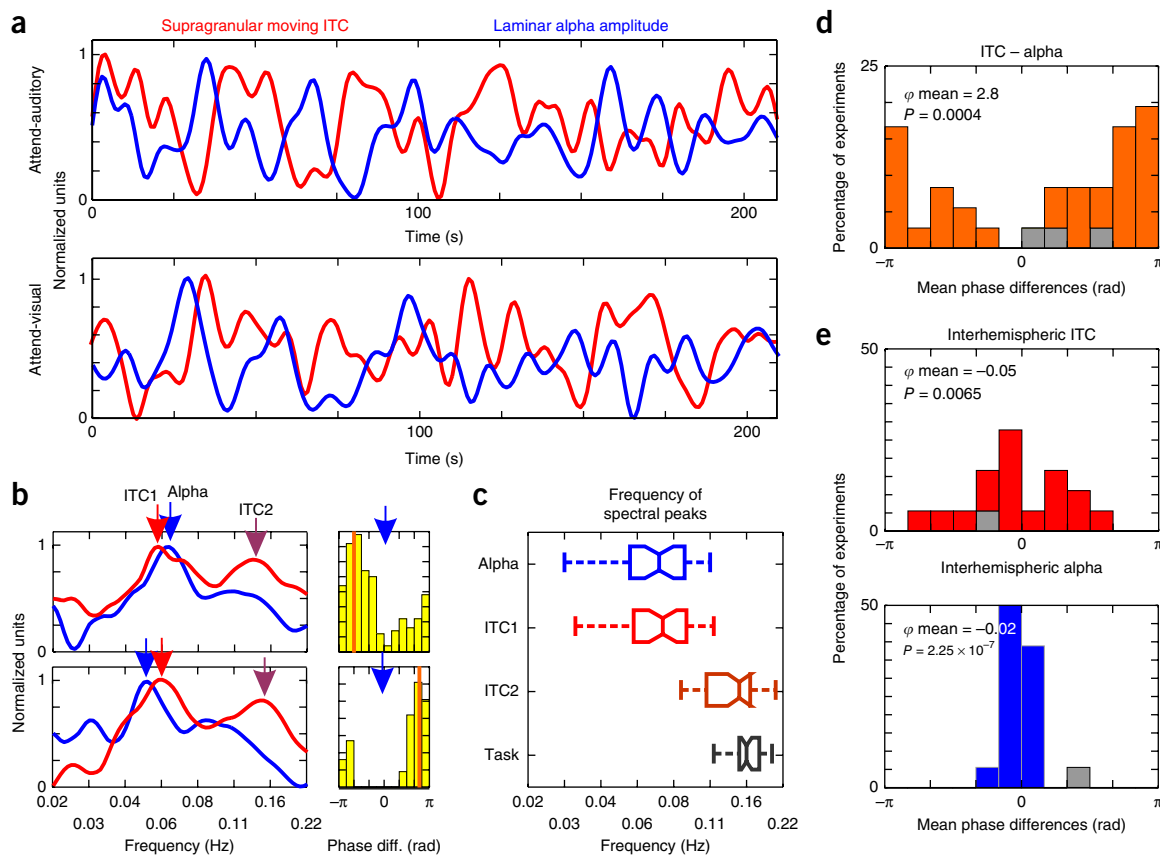


**Figure 4** Slow counterphase fluctuation of delta oscillatory entrainment and alpha amplitude. **(a)** Low-pass-filtered supragranular moving ITC and cross-laminar alpha amplitude waveforms from a representative attend-auditory (top) and attend-visual (bottom) trial block (same blocks as in **Fig. 3a**). **(b)** Representative spectra of supragranular moving ITC and cross-laminar alpha amplitude from two experiments. Red and maroon arrows denote prominent peaks in the spectrum of moving ITC (ITC1 and ITC2, respectively); blue arrows denote prominent peaks in the spectrum of moving alpha amplitude signals. Histograms to the right display the distribution of ITC – alpha phase differences at the frequency of the alpha spectrogram peak throughout the trial blocks. The orange lines denote the mean phases of the phase distributions. **(c)** Frequency of moving alpha (blue) and moving ITC spectral peaks (red, lower-frequency peak; maroon, higher-frequency peak) and the task frequency (black) from all trial blocks. The boxplots have lines at lower quartile, median, and upper quartile values, while whiskers show the extent of the data. **(d)** ITC – alpha mean phase differences pooled across experiments are significantly biased ( $n = 36$ , Rayleigh test;  $P$ -value and mean phase ( $\phi$ ) are displayed in the figure). Grey, mean phases of nonsignificantly biased phase distributions. **(e)** The distributions of ITC – ITC (top) and alpha – alpha (bottom) mean phase differences derived from concurrently recorded left and right hemisphere A1 neuronal ensemble activity indicate synchronous modulation across hemispheres ( $n = 18$ , Rayleigh test).

verified these findings: while the effect of entrainment (ITCa, ITCv or no-ITC) was significant for delta ( $F_{2,210} = 146.95$ ,  $P = 1.22 \times 10^{-40}$ ), theta ( $F_{2,210} = 3.95$ ,  $P = 0.02$ ) and gamma oscillations ( $F_{2,210} = 5.18$ ,  $P = 0.006$ ), the effect of cueing (attend-auditory versus attend-visual) was not significant in any of the frequency bands (delta:  $F_{1,210} = 0.47$ ,  $P = 0.49$ ; theta:  $F_{1,210} = 1.49$ ,  $P = 0.22$ ; alpha:  $F_{1,210} = 0.47$ ,  $P = 0.49$ ; beta:  $F_{1,210} = 0.34$ ,  $P = 0.56$ ; gamma:  $F_{1,210} = 3.13$ ,  $P = 0.07$ ). There was no interaction of entrainment and cueing (delta:  $F_{2,210} = 0.1$ ,  $P = 0.90$ ; theta:  $F_{2,210} = 0.69$ ,  $P = 0.5$ ; alpha:  $F_{2,210} = 0.1$ ,  $P = 0.9$ ; beta:  $F_{2,210} = 0.06$ ,  $P = 0.93$ ; gamma:  $F_{2,210} = 0.04$ ,  $P = 0.96$ ). These results verify and extend previous observations that selective attention to a given modality is indexed by the phase reset of oscillations in the delta, theta and gamma frequency bands, while ignoring stimuli (attending to a different modality) and attentional lapses are both characterized by a lack of phase reset.

Next, we compared oscillatory amplitudes and found that cueing, as in the case of ITC had no effect on them (two-way ANOVA; delta:  $F_{1,210} = 0.22$ ,  $P = 0.63$ ; theta:  $F_{1,210} = 0.13$ ,  $P = 0.71$ ; alpha:  $F_{1,210} = 0.02$ ,  $P = 0.88$ ; beta:  $F_{1,210} = 0.0008$ ,  $P = 0.97$ ; gamma:  $F_{1,210} = 0.01$ ,  $P = 0.9$ ). These results suggest that the quality of the three distinct attentional

states did not differ in the two different cueing contexts; cueing merely increased the length of attention to the cued modality stimuli (see above). As opposed to the effect of cueing, comparing amplitude values across the different frequency bands revealed that entrainment had a significant effect on amplitudes in the alpha, beta and gamma frequency bands (alpha:  $F_{2,210} = 20.86$ ,  $P = 6.6 \times 10^{-8}$ ; beta:  $F_{2,210} = 10.95$ ,  $P = 1.2 \times 10^{-4}$ ; gamma:  $F_{2,210} = 11.73$ ,  $P = 2.7 \times 10^{-5}$ ). As **Figure 3c** illustrates, in contrast to ITC measures, there appeared to be no amplitude differences between auditory (ITCa) versus visual entrainment conditions (ITCv). Rather, alpha, beta and gamma amplitudes were greater during periods that lacked entrainment (noITC). To estimate the laminar location of these amplitude differences, we aligned laminar spectral amplitude profiles across all experiments (Online Methods) and statistically compared amplitude differences during entrainment versus no-entrainment periods (**Fig. 3d**). Since we found no effect of cueing on any spectral measures across the three different entrainment conditions (as described above), we merged the data recorded in attend-auditory and attend-visual trial blocks. We found that increased alpha–beta–gamma amplitudes during no-entrainment time periods were widespread across the different cortical layers. Our layer-specific

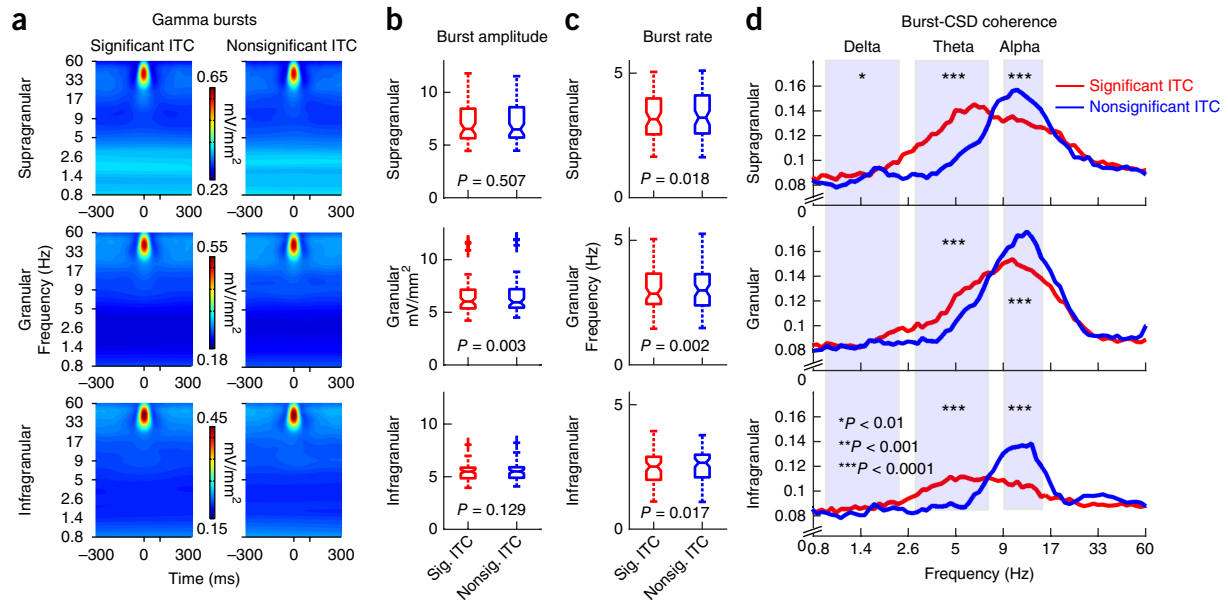


**Figure 5** Entrainment-correlated patterns of cross-frequency coupling. (a) Time–frequency amplitude maps show gamma bursts averaged across all experiments during time periods of entrainment (significant ITC, left) and no entrainment (nonsignificant ITC, right) from the different cortical layers. (b) Gamma burst amplitudes pooled across all experiments and cueing conditions during significant ITC (red, sig. ITC) and nonsignificant ITC (blue, nonsig. ITC) time periods only show a significant difference in the granular layer ( $n = 72$ , Wilcoxon signed-rank tests). The boxplots have lines at lower quartile, median, and upper quartile values, while whiskers show the extent of the data. (c) The rate of gamma bursts in different layers during significant ITC (red) and nonsignificant ITC (blue) time periods shows a significant difference across all layers ( $n = 72$ , Wilcoxon signed-rank tests). As in **b**, boxplots have lines at lower quartile, median, and upper quartile values, while whiskers show the extent of the data. (d) Layer-specific burst-CSD coherence spectra. Stars denote significant differences in the delta, theta and alpha frequency ranges in significant ITC versus nonsignificant ITC periods ( $n = 72$ , Wilcoxon signed-rank tests; supragranular:  $P_{\text{delta}} = 0.0014$ ,  $P_{\text{theta}} = 8.1 \times 10^{-12}$ ,  $P_{\text{alpha}} = 5.5 \times 10^{-5}$ ; granular:  $P_{\text{delta}} = 0.03$ ,  $P_{\text{theta}} = 1.5 \times 10^{-5}$ ,  $P_{\text{alpha}} = 2.6 \times 10^{-5}$ ; infragranular:  $P_{\text{delta}} = 0.09$ ,  $P_{\text{theta}} = 2.9 \times 10^{-5}$ ,  $P_{\text{alpha}} = 2 \times 10^{-6}$ ).

amplitude maps also revealed a countersign change in delta amplitude at the frequency of auditory (ITCa versus noITC) and visual stimulus repetition rate (ITCv versus noITC), but only in the supragranular layers (**Fig. 3d**). This latter finding in the supragranular layers can be explained by the presence of greater delta energy at the frequency of entrainment<sup>20</sup>; therefore, in the following we will focus only on the alpha–beta–gamma effect.

### Slow counterphase oscillatory dynamics

Our results showed that alpha amplitude across all cortical layers increased during periods that lacked entrainment to stimulus streams. Therefore, it was not surprising that we found a countersign modulation by overlaying moving delta ITC and alpha amplitude (**Fig. 4a**): whenever delta ITC was high, alpha amplitude was low and vice versa. What was unexpected was that this countersign modulation appeared to be rather rhythmic throughout the entire trial block, and that it seemed slower than the rhythm of the task (defined as the average frequency of target stimulus occurrence, i.e., 0.16 Hz). To quantify these observations, we first calculated the spectra of moving delta ITC and alpha waveforms. As the examples in **Figure 4b** illustrate, both ITC and alpha spectra exhibited prominent peaks around 0.06 Hz, and the ITC spectra displayed a second peak around 0.15 Hz. This second peak was often absent from the moving alpha amplitude spectra. As the pooled data show (**Fig. 4c**), the prominent lower-frequency peaks in moving ITC and alpha amplitude spectra were not significantly different from each other across all experiments ( $n = 36$ , Wilcoxon signed-rank test,  $P = 0.19$ ), but both were significantly different from the task frequency ( $n = 36$ , Wilcoxon signed rank test,  $P_{\text{ITC}} = 3.64 \times 10^{-7}$ ,  $P_{\text{alpha}} = 3.99 \times 10^{-7}$ ). The higher-frequency peak detectable in the delta ITC spectrum was, on the other hand, not significantly

different from the task frequency ( $n = 36$ , Wilcoxon signed rank test,  $P = 0.072$ ). These results indicate that the most prominent fluctuation of attention, indexed by opposing modulation of entrainment and alpha amplitude, was independent of the task structure.

To determine whether the time courses of moving ITC and alpha amplitude waveforms were anticorrelated as their countersign modulation suggested, we measured the amount of bias in the distribution of their phase differences (coherence) at the frequency of the dominant peak in the alpha amplitude spectrum. We found significant coherence (Rayleigh  $P < 0.05$ ) of moving ITC and moving alpha amplitude waveforms in 33 out of 36 experiments. As **Figure 4d** shows, mean phase differences (ITC versus alpha) were significantly biased toward a half-oscillatory cycle, which verified the anticorrelated delta ITC–alpha amplitude relationship.

To test whether moving ITC and alpha reflected local or more global long-timescale fluctuations of neuronal dynamics, we calculated the coherence of moving ITC and alpha amplitude waveforms in simultaneous left and right hemisphere recordings (**Fig. 4e**). We found that all but one set of paired recordings displayed coherent (Rayleigh  $P < 0.05$ ) interhemispheric delta ITC and alpha amplitude fluctuations, with mean phase difference distributions significantly biased toward zero. This indicates that both delta ITC and alpha amplitude were modulated synchronously across hemispheres, indicative of the involvement of large-scale networks rather than local neuronal ensemble mechanisms in the orchestration of anticorrelated entrainment–alpha amplitude fluctuation.

### Distinct delta–theta versus alpha–beta referenced operational modes

As **Figure 3c,d** shows, besides the alpha amplitude increase, the amplitude of beta and gamma oscillations also increased during periods

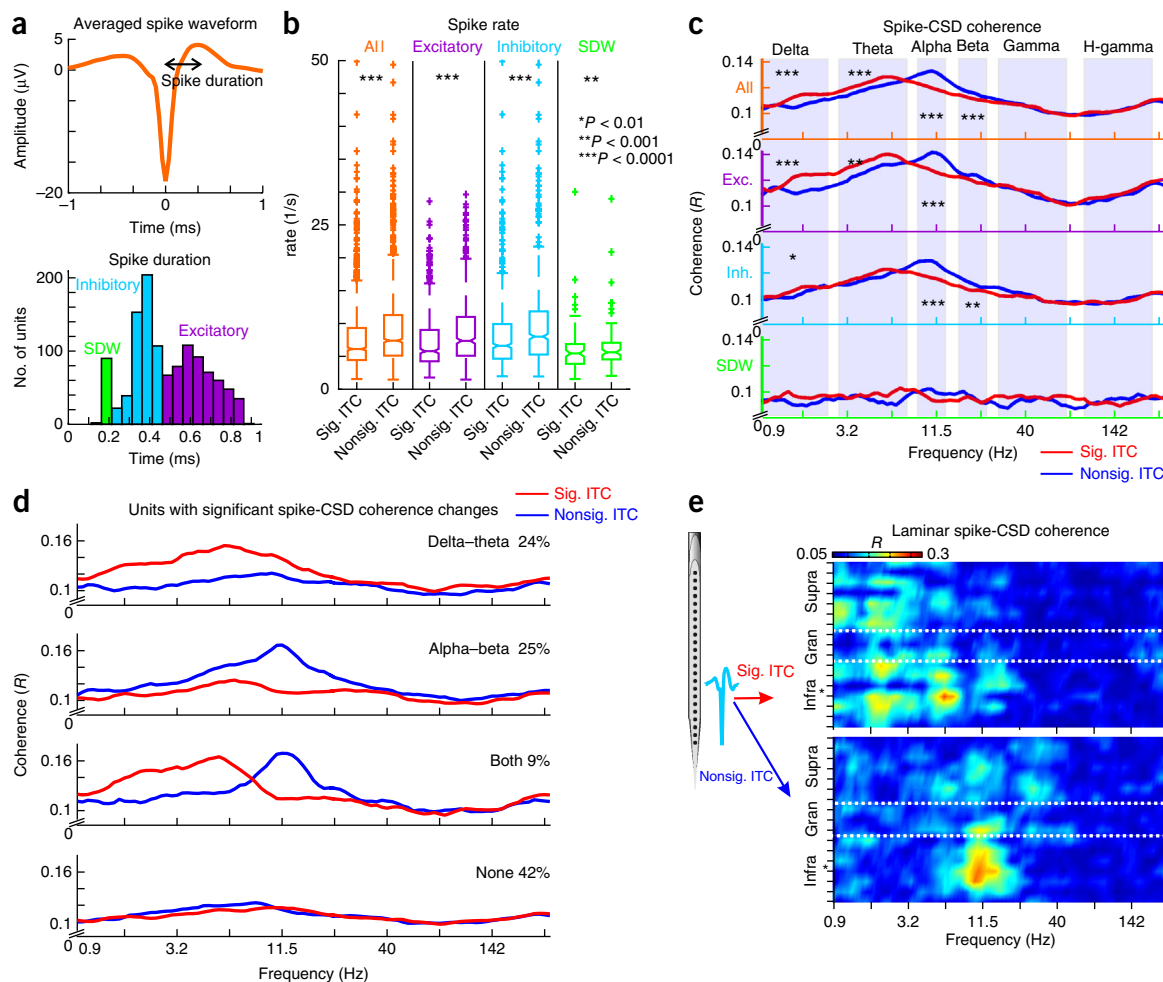


**Figure 6** Distinct brain-state-dependent patterns of single-unit activity. **(a)** Top: spike waveform averaged across all single units ( $n = 1,167$ ). Spike duration was measured as the time between the negative peak used to detect and align spikes and the subsequent positive peak. Bottom: distribution of spike durations. Putatively, short, medium and long spike durations represent afferent spikes (SDW), firing of inhibitory neurons and firing of excitatory neurons, respectively. **(b)** Pooled spike rates of all neurons (orange) and the different unit types during significant ITC (sig. ITC) and nonsignificant ITC (nonsig. ITC) time periods. Stars denote significant firing rate increases during nonsignificant ITC periods ( $n_{\text{all}} = 1,167$ ,  $n_{\text{inhibitory}} = 589$ ,  $n_{\text{excitatory}} = 490$ ,  $n_{\text{SDW}} = 88$ , Wilcoxon signed-rank tests,  $P_{\text{all}} = 2.5 \times 10^{-123}$ ,  $P_{\text{excitatory}} = 4.9 \times 10^{-55}$ ,  $P_{\text{inhibitory}} = 5.5 \times 10^{-65}$ ,  $P_{\text{SDW}} = 8.1 \times 10^{-4}$ ). The boxplots have lines at lower quartile, median, and upper quartile values, while whiskers show the extent of the data. **(c)** Unit specific spike-CSD coherence spectra during significant ITC (red) versus nonsignificant ITC (blue) periods. Stars denote significant differences in the frequency ranges marked by shaded regions ( $n_{\text{all}} = 1,167$ ,  $n_{\text{inhibitory}} = 589$ ,  $n_{\text{excitatory}} = 490$ ,  $n_{\text{SDW}} = 88$ , Wilcoxon signed-rank tests; all:  $P_{\text{delta}} = 1.5 \times 10^{-6}$ ,  $P_{\text{theta}} = 3.3 \times 10^{-5}$ ,  $P_{\text{alpha}} = 2.4 \times 10^{-20}$ ,  $P_{\text{beta}} = 9.2 \times 10^{-5}$ ,  $P_{\text{gamma}} = 0.72$ ,  $P_{\text{H-gamma}} = 0.08$ ; excitatory:  $P_{\text{delta}} = 8.3 \times 10^{-6}$ ,  $P_{\text{theta}} = 9.3 \times 10^{-4}$ ,  $P_{\text{alpha}} = 1.1 \times 10^{-7}$ ,  $P_{\text{beta}} = 0.055$ ,  $P_{\text{gamma}} = 0.33$ ,  $P_{\text{H-gamma}} = 0.0197$ ; inhibitory:  $P_{\text{delta}} = 0.002$ ,  $P_{\text{theta}} = 0.015$ ,  $P_{\text{alpha}} = 1.9 \times 10^{-13}$ ,  $P_{\text{beta}} = 6.1 \times 10^{-4}$ ,  $P_{\text{gamma}} = 0.062$ ,  $P_{\text{H-gamma}} = 0.75$ ; SDW:  $P_{\text{delta}} = 0.45$ ,  $P_{\text{theta}} = 0.27$ ,  $P_{\text{alpha}} = 0.02$ ,  $P_{\text{beta}} = 0.27$ ,  $P_{\text{gamma}} = 0.28$ ,  $P_{\text{H-gamma}} = 0.71$ ). Exc., excitatory; inh., inhibitory; H-gamma, high-gamma. **(d)** Traces depict averaged spike-CSD coherence spectra of units with (top) a significant delta–theta band spike-CSD coherence increase during significant ITC periods, (upper middle) spike-CSD coherence spectra of units with a significant alpha-beta spike-CSD coherence decrease during the same periods, (lower middle) spike-CSD coherence spectra of units that display entrainment correlated coherence changes in both frequency bands and (bottom) units that show no significant coherence change. **(e)** Laminar spike-CSD coherence spectra of a putative inhibitory neuron from the infragranular layers (location marked by the star) during significant ITC (top) and nonsignificant ITC (bottom) time periods. Gran, granular; infra, infragranular; supra, supragranular.

of attentional lapses when delta oscillations were not entrained by any of the sensory stimulus streams. The observation of increased beta amplitudes during no-entrainment periods characterized by high amplitude alpha oscillatory activity is in line with previous findings indicating that alpha and beta oscillations are comodulated in time and colocalized in space<sup>25–28</sup> and therefore seem to support similar neuronal operations. However, our finding that gamma amplitude was also higher during periods characterized by increased alpha was unexpected, since alpha is usually associated with suppression and gamma is typically an indicator of excitability. Hence, high alpha amplitudes should result in suppressed gamma-frequency-band neuronal activity,

which is what prior studies have found<sup>29–31</sup>. This discrepancy led us to further investigate the gamma amplitude enhancement that occurred during no-entrainment time periods. Since it is well documented that, rather than being continuous, gamma-band neuronal activity occurs in bursts<sup>30</sup>, we decided to examine the properties of gamma bursting during entrainment (significant ITC) versus no-entrainment (nonsignificant ITC) periods (Fig. 5). We first tested the peak frequency of gamma bursts in distinct cortical layers, and found no effect of entrainment across trial blocks ( $n = 72$ , Wilcoxon signed-rank test:  $P_{\text{supragranular}} = 0.6$ ,  $P_{\text{granular}} = 0.38$ ,  $P_{\text{infragranular}} = 0.93$ ). In contrast, we found a significant increase in the amplitude of gamma bursts

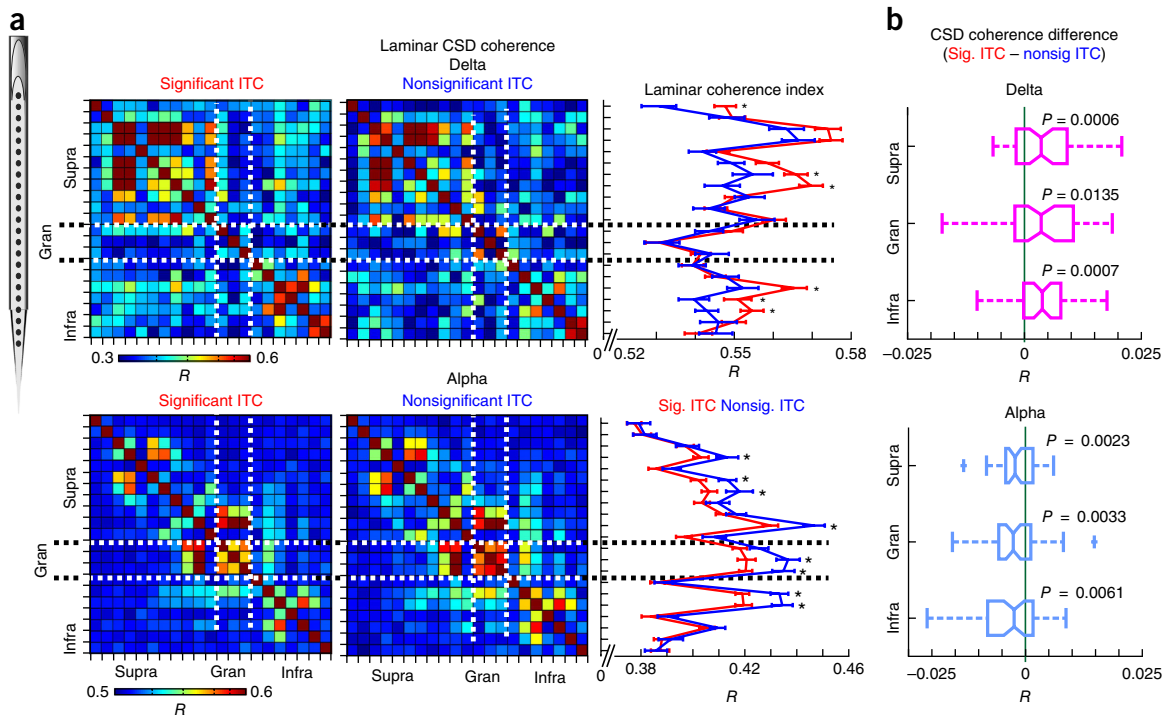


**Figure 7** Entrainment-correlated changes in laminar delta and alpha coherence. (a) Laminar delta (top) and alpha (bottom) coherence matrices calculated during significant ITC (left) and nonsignificant ITC (right) time periods. Traces to the right show coherence values ( $R$ ) averaged along one dimension; error bars depict mean  $\pm$  standard error. Stars, significant differences between significant ITC (sig. ITC, red) and nonsignificant ITC (nonsig. ITC, blue) periods ( $n_{\text{sig. ITC}} = 137$ ,  $n_{\text{noITC}} = 61$ , Wilcoxon rank sum,  $P < 0.01$ ). (b) Layer-specific difference of delta (magenta) and alpha (blue) coherence ( $R$ ) between significant ITC and nonsignificant ITC periods. The boxplots have lines at lower quartile, median, and upper quartile values, while whiskers show the extent of the data.  $P$ -values denote statistical significance for each distribution's difference from 0, which would indicate no change ( $n = 72$ , one sample  $t$ -test, d.f. = 71,  $t_{\text{delta-supragranular}} = 4.49$ ,  $t_{\text{delta-granular}} = 3.18$ ,  $t_{\text{delta-infragranular}} = 3.91$ ,  $t_{\text{alpha-supragranular}} = -3.25$ ,  $t_{\text{alpha-granular}} = -3.97$ ,  $t_{\text{alpha-infragranular}} = -2.71$ ). Gran, granular; infra, infragranular; supra, supragranular.

during no-entrainment time periods in the granular layer (Fig. 5b). Additionally, we found that the rate at which gamma bursts occurred was significantly increased across all layers during no-entrainment time periods (Fig. 5c), which, together with the burst amplitude increase in the granular layer, could account for the gamma amplitude increase observed in the averaged laminar profiles (Fig. 3d).

The distinction between the amplitude and rate of gamma bursting is important since the gamma amplitude differences observed in the time-averaged data (Fig. 3d) do not have to be directly related to changes in gamma amplitude *per se*, but rather could be due to the restructuring of gamma bursts. Therefore, we examined whether increased gamma rates could be associated with changes in cross-frequency coupling by measuring how the timing of gamma bursts correlated with the phase of neuronal ensemble activity at lower frequencies. Figure 5d shows averaged burst-CSD coherence spectra from the supragranular, granular and infragranular layers. Higher values indicate stronger gamma-burst-CSD coupling at a given frequency. We found notable countersign differences in gamma burst-theta phase and gamma burst-alpha phase coupling. While theta-gamma and, to a lesser degree, delta-gamma phase-amplitude coupling dominate during periods of entrainment, especially in the supragranular layers, during no-entrainment periods alpha-gamma coupling takes over in all cortical layers. Thus, phase amplitude coupling undergoes radical changes during switches between delta-entrainment and high-alpha dominated brain states.

Since gamma-frequency neuronal activity and multiunit activity usually display correlated amplitude changes, we tested whether

MUA increased as gamma did during no-entrainment time periods. We found that indeed, MUA of all cortical layers was significantly greater during no-entrainment periods ( $n = 72$ , Wilcoxon signed-rank test;  $P_{\text{supragranular}} = 0.0264$ ,  $P_{\text{granular}} = 0.0043$ ,  $P_{\text{infragranular}} = 0.0019$ ), which is again a counterintuitive finding in light of the commonly accepted suppressive role of alpha oscillatory activity. Therefore, we decided to further dissect the MUA amplitude effect by characterizing single-unit firing properties during entrainment and no-entrainment periods.

We isolated 1,167 single units from the 36 A1 multielectrode recordings. Figure 6a shows the distribution of spike durations as defined by peak-to-trough time, with three obvious peaks. Based on previous studies examining the detailed differences in spike waveform and spike train statistics<sup>32–35</sup>, the long- and medium-duration waveforms likely correspond predominantly to the spiking of putative excitatory neurons and inhibitory neurons, respectively. While short-duration waveforms (SDWs) are not often isolated, a recent study suggests that these might reflect afferent spiking activity<sup>35</sup>. We arbitrarily assigned parts of the distribution to these categories, acknowledging that there is likely considerable overlap between the groups with different spike durations. Nevertheless, in line with the literature, median spike rates were significantly higher in the putative inhibitory neuron group compared to both other groups ( $n_{\text{inhibitory}} = 589$ ,  $n_{\text{excitatory}} = 490$ ,  $n_{\text{SDW}} = 88$ , Wilcoxon rank sum,  $P_{\text{inhibitory-excitatory}} = 2.33 \times 10^{-4}$ ,  $P_{\text{inhibitory-SDW}} = 4.09 \times 10^{-11}$ ). Figure 6b shows firing rates during entrainment (significant ITC) versus no-entrainment (nonsignificant ITC) periods for all neurons, as well as separately for the different

putative cell types. We found that all neuronal groups displayed significantly increased firing rates during no-entrainment periods. This corroborates our MUA result and raises the question: as with gamma bursts, do increased firing rates reflect distinct spike-CSD coherence patterns? The pooled data displayed in **Figure 6c** indicates that this is indeed the case. If we consider all neurons, delta–theta spike-CSD coherence is greater during entrainment, while alpha–beta spike-CSD coherence dominates no-entrainment periods. Whereas across different brain states, delta–theta–alpha effects dominate in putative excitatory neurons, alpha–beta spike-CSD coherence changes dominate in putative inhibitory interneurons. We found neither distinct spike-CSD coherence patterns nor any entrainment-related changes in the case of SDWs. These results indicate that in general, the firing of A1 neurons is structured dominantly by delta–theta oscillatory activity during selective attention to rhythmic external stimuli, and to alpha–beta oscillatory activity during lapses of attention.

The repetitive combination technique used when calculating spike-CSD coherences enabled us to detect significant differences of spike-CSD coherence between entrainment and no-entrainment periods for every single unit (Online Methods). We found that 24% of all units displayed a significant delta–theta spike-CSD coherence increase during entrainment, 25% displayed a significant alpha–beta spike-CSD coherence increase during no-entrainment periods and 9% displayed both (**Fig. 6d**; Wilcoxon signed-rank tests,  $P < 0.01$ ; Online Methods). If spike-CSD coherence indicates how strongly a given neuron is integrated in synchronous neuronal ensemble operations orchestrated by neuronal oscillations, this result might mean that while certain neurons are recruited during attentive brain states, others are used more during attentional lapses, with a proportion being able to switch between operational modes.

Besides calculating local spike-CSD coherences, we also calculated laminar spike-CSD profiles, as shown in **Figure 6e**. These profiles revealed strikingly different coherence patterns during entrainment versus no-entrainment periods, and not just in frequency but also in cortical space. Therefore, we decided to investigate the laminar coherence patterns that characterize entrainment versus no-entrainment brain states, since these likely reflect differing functional connectivity patterns that funnel the effect of neuronal spiking toward differing neuronal computations.

**Figure 7a** shows representative laminar coherence matrices displaying delta and alpha CSD coherence across all electrode pairs during periods of entrainment (significant ITC) versus no-entrainment (nonsignificant ITC). It is apparent that while the networks delineated by delta and alpha coherence patterns overlapped, they also showed distinct characteristics. Delta coherence was strongest within and across supragranular and infragranular sites, while alpha coherence highlighted interconnected nodes within all cortical layers. The differences between entrainment and no-entrainment conditions might not be obvious from the coherence matrices, so we averaged coherence values along one spatial dimension, creating a one-dimensional laminar coherence index (**Fig. 7a**). This index describes, for each recording location, how strongly neuronal activity was coherent with neuronal activity at all other locations. As the representative example in **Figure 7a** shows, there were substantial countersign differences in delta and alpha cross-laminar coherence between entrainment and no-entrainment brain states. While supragranular and infragranular delta coherence increased during entrainment, alpha coherence across all layers increased during no-entrainment periods. Interestingly, while in the majority of individual laminar coherence profiles, like in **Figure 7a**, delta coherence differences were not significant in the granular layer, the difference was significant in the pooled data (**Fig. 7b**).

To summarize, while interlaminar delta coherence was stronger during attention to rhythmic stimulus streams, alpha coherence across cortical layers was stronger during lapses of attention, revealing differing interlaminar functional connectivity patterns specific to delta and alpha oscillations respectively, resulting in the distinct routing of information.

## DISCUSSION

We found that the entrainment of neuronal oscillations supporting the selection and attentive processing of rhythmic stimulus streams<sup>7,19–21</sup> was far from stable during the performance of a continuous selective attention task. Lapses of entrainment occurred at regular, 10–30-s time intervals, corresponding to lapses of attention and behavioral responding. While periods of oscillatory entrainment were characterized by delta–theta frequency patterning of gamma oscillatory activity (**Fig. 5d**) and neuronal firing (**Fig. 6c**), lapses of entrainment were characterized by increased amplitude alpha oscillations and alpha-frequency band patterning of high-frequency neuronal ensemble (**Fig. 5d**) and single-neuron activity (**Fig. 6c**). Together with divergent variations in interlaminar cortical coherence between entrainment and no-entrainment brain states (**Fig. 7**), these data outline two distinct operational modes of auditory cortical neuronal populations that likely subservise distinct perceptual–cognitive functions. The counterphase fluctuation of neuronal dynamics we detected in primary auditory cortex bears striking similarities to the counterphase fluctuation of resting-state oscillations detected by neuroimaging studies<sup>10</sup> and their correlation to alpha–beta frequency-band electroencephalographic activity in humans<sup>36,37</sup>. We therefore propose that the distinct neuronal-ensemble and single-neuron dynamics described by our study reflect the linking of auditory cortex machinery to task-positive (entrainment) versus task-negative (high alpha) large-scale functional networks.

We also found that the slow counterphase modulation of entrainment versus no-entrainment periods was independent of the temporal structure of the task (**Fig. 4c**). This indicates that the slow fluctuations of neuronal dynamics observed in our study are orchestrated by internally timed mechanisms, which is why we argue that this fluctuation can be linked to large-scale functional networks detected in neuroimaging studies<sup>9–11</sup>. While anticorrelations in functional MRI (fMRI) signals have been proposed to be simply an artifactual consequence of global signal regression<sup>38</sup>, our electrophysiological findings provide confirmation that counterphase modulations of the patterning of neuronal activity do occur in cortical neuronal ensembles on temporal scales that are comparable to the low-frequency fluctuations identified by neuroimaging studies. Alternatively, as a recent study by van den Brink *et al.*<sup>39</sup> demonstrated, periods of no-entrainment observed in our data could occur following behavioral errors. However, since the overall false alarm rate was low in our study (**Fig. 1b**) and in some trial blocks false alarms did not occur at all (**Fig. 3b**), this explanation is unlikely. Nevertheless, the second, higher-frequency peak in the moving ITC spectrum, which corresponds to the rate at which targets occurred (**Fig. 4b,c**), might be due to a similar process that distracts from the current task and diminishes entrainment temporarily following target stimuli.

Despite our subjects' poor behavioral performance during the no-entrainment, high-alpha-amplitude periods, our data challenge the notion that alpha oscillations merely reflect suppression if gamma oscillatory amplitudes and neuronal firing rates are taken as indicators of neuronal ensemble excitability, since we found that both of these increased during the high-alpha-amplitude brain state. This seems to indicate that in addition to controlling excitability,

the main role of neuronal oscillations—including alpha—is to impose differing activity patterns on neuronal ensembles, a side effect of which might be impairment in responding to stimuli. These contrasting activity patterns in turn likely promote distinct brain operations, like active sensing versus internal information processing and corresponding bottom-up versus top-down dominated information flow. Interestingly, Haegens and colleagues<sup>40</sup> also found an overall firing rate increase during the highest alpha amplitude periods in primary somatosensory cortex but not in secondary somatosensory or motor cortices, indicating that primary cortices might differ from other regions in alpha-related effects. Alternatively, since there is overwhelming evidence that the brain does utilize alpha oscillations to suppress cortical regions that are irrelevant for goal-directed sensory processing (for a review see ref. 41), it is possible that this most commonly detected ‘suppressive alpha’ is different from the ‘timing alpha’ described by our study and the study of Saalman and colleagues<sup>42</sup>. We speculate that the only reason functionally different alpha rhythms occupy the same frequency space is that they are both referenced to internal timing mechanisms (pacemaker neurons or microcircuits) and not to external stimuli or the pattern of their sampling like delta–theta oscillations. Womelsdorf and colleagues<sup>43</sup> also suggest that there are at least two different types of alpha rhythms in sensory cortices: an infragranularly initiated suppressive alpha and a pulvinar-initiated alpha that is meant to enhance relevant information. They speculate that the cortical signature of this latter alpha operational mode should be widespread alpha–gamma cross-frequency coupling involving all cortical layers, which is what our study found during periods when delta rhythms were not entrained by sensory stimuli. Our data provide strong support for the hypothesis that different brain states are characterized by distinct dynamic motifs<sup>43</sup> that likely support differing effective connectivity patterns and thereby neuronal computations subserving the selection and integration of relevant information.

The finding that different neurons preferentially synchronize their firing to local neuronal-ensemble oscillations, either during entrainment or during periods dominated by alpha oscillations, indicates that by changing the frequency of its neuronal ensemble oscillations, the brain might be able to engage distinct neuronal populations. We found that while some neurons preferentially fire on certain phases of local delta–theta neuronal ensemble oscillations during entrainment, others synchronize their firing to neuronal ensemble oscillations only during high-alpha operational modes (Fig. 6d). This is likely due to the different neurons’ or neuronal ensembles’ resonance properties, as determined by their cellular properties and/or connectivity patterns<sup>43,44</sup>. A relatively small portion (9%) of neurons we detected could synchronize their firing both to delta–theta and alpha–beta neuronal ensemble oscillations, possibly due to their less-sharply-tuned cellular-network resonance properties. We hypothesize that when neurons do not synchronize their firing to synchronous neuronal ensemble rhythms, the effect of their firing is diminished and they are excluded from neuronal computations due to the lack of ‘functional convergence’ on their target neurons. Thus, even though they fire at the same or even higher rate during different brain states, their action potentials will not be taken into account for the currently relevant brain operation. While future modeling and single cell studies are needed to verify this scenario, our data provide strong support for the notion that by simply switching the frequency at which cortical neuronal ensembles oscillate, distinct neuronal groups can be recruited and effectively connected by distinct intralaminar and interlaminar oscillatory patterns.

In the introduction we attributed short-timescale oscillations in neuronal ensembles as a means for maintaining an ideal excitability state while conserving energy<sup>1</sup>. Along this line of thought,

what might the long-timescale variations of neuronal ensemble dynamics uncovered by our study and numerous prior studies be meant to maintain? Based on our current results, we propose that they maintain an ideal balance of delta–theta entrainment-dominated externally oriented versus alpha–beta dominated internally oriented information processing. If true, ultra-slow resting state oscillations maintaining this perceptual–cognitive balance likely exist so that brain operations are not ‘captured’ by the external or internal environment for long periods of time. For example, the unavoidable return of the alpha-dominated brain state during selective attention would allow for detaching from external stimulation, re-evaluating current goals and updating the cognitive context in which external stimuli are evaluated. In this theoretical framework, if this detaching mechanism overacts, the brain simply cannot connect to the external world, which might be the underlying cause of the lack of entrainment in schizophrenia<sup>45</sup>. In fact, several recent neuroimaging studies provide evidence that the task-negative default mode network is indeed overactive in schizophrenia patients<sup>46,47</sup> and that this is accompanied by increased alpha-frequency-band neuronal activity in the same regions<sup>48</sup>.

As we previously proposed<sup>49</sup>, the two hubs orchestrating externally directed (entrainment) versus internally directed (high alpha) information processing dynamics could be core-matrix organized thalamic relay nuclei and the pulvinar, respectively, with the thalamic reticular nucleus balancing their influence in counterphase. While this hypothesis needs to be tested, it is plausible that impairments at any node of this large-scale thalamocortical system maintaining the perceptual–cognitive balance would lead to psychiatric and neurodevelopmental disorders, like schizophrenia and attention deficit hyperactivity disorder. Global dynamics of the moving ITC measure used in our study could provide a useful tool to aid diagnosis in these cases, and since moving ITC enables tracking attention practically in real-time, it could also provide a basis for closed-loop biofeedback therapeutic techniques, or training of attention<sup>50</sup>. In addition, this measure might prove to be an extremely useful tool in assessing attention in subjects who cannot cooperate easily, like infants and people with autism.

To summarize, we identified two distinct, counterphase fluctuating brain states in the auditory cortex of subjects performing a selective intermodal attention task. These brain states were characterized by distinct neuronal dynamics, one framed by oscillations adapting to the temporal structure of external events and one by alpha oscillations, providing an externally linked versus internally linked temporal reference frame for the coordination of neuronal computations. The slow fluctuation of these two brain states likely reflects the counterphase modulation of task-positive and task-negative large-scale networks, which we propose is meant to maintain an ideal perceptual–cognitive balance.

## METHODS

Methods, including statements of data availability and any associated accession codes and references, are available in the [online version of the paper](#).

*Note: Any Supplementary Information and Source Data files are available in the online version of the paper.*

## ACKNOWLEDGMENTS

Support for this work was provided by NIH grant R01DC012947 from the NIDCD (P.L.) and R01MH109289 from the NIMH (D.C.J.).

## AUTHOR CONTRIBUTIONS

P.L. and M.N.O. designed the study. M.N.O., T.M. and D.R. performed the experiments. P.L. and D.C.J. designed the analyses. P.L., M.N.O., A.B. and S.A.N. performed the analyses. P.L. wrote the manuscript with input from all authors.

## COMPETING FINANCIAL INTERESTS

The authors declare no competing financial interests.

Reprints and permissions information is available online at <http://www.nature.com/reprints/index.html>.

1. Buzsáki, G. *Rhythms of the Brain* (Oxford Univ. Press, 2006).
2. Fries, P. Rhythms for cognition: communication through coherence. *Neuron* **88**, 220–235 (2015).
3. Gray, C.M., König, P., Engel, A.K. & Singer, W. Oscillatory responses in cat visual cortex exhibit inter-columnar synchronization which reflects global stimulus properties. *Nature* **338**, 334–337 (1989).
4. Dragoi, G. & Buzsáki, G. Temporal encoding of place sequences by hippocampal cell assemblies. *Neuron* **50**, 145–157 (2006).
5. O'Keefe, J. & Conway, D.H. Hippocampal place units in the freely moving rat: why they fire where they fire. *Exp. Brain Res.* **31**, 573–590 (1978).
6. Buschman, T.J. & Miller, E.K. Top-down versus bottom-up control of attention in the prefrontal and posterior parietal cortices. *Science* **315**, 1860–1862 (2007).
7. Lakatos, P., Karmos, G., Mehta, A.D., Ulbert, I. & Schroeder, C.E. Entrainment of neuronal oscillations as a mechanism of attentional selection. *Science* **320**, 1118–1123 (2008).
8. Womelsdorf, T., Fries, P., Mitra, P.P. & Desimone, R. Gamma-band synchronization in visual cortex predicts speed of change detection. *Nature* **439**, 733–736 (2006).
9. Biswal, B., Yetkin, F.Z., Haughton, V.M. & Hyde, J.S. Functional connectivity in the motor cortex of resting human brain using echo-planar MRI. *Magn. Reson. Med.* **34**, 537–541 (1995).
10. Fox, M.D. *et al.* The human brain is intrinsically organized into dynamic, anticorrelated functional networks. *Proc. Natl. Acad. Sci. USA* **102**, 9673–9678 (2005).
11. Weissman, D.H., Roberts, K.C., Visscher, K.M. & Woldorff, M.G. The neural bases of momentary lapses in attention. *Nat. Neurosci.* **9**, 971–978 (2006).
12. Allers, K.A. *et al.* Multisecond periodicities in basal ganglia firing rates correlate with theta bursts in transcortical and hippocampal EEG. *J. Neurophysiol.* **87**, 1118–1122 (2002).
13. de Pasquale, F. *et al.* Temporal dynamics of spontaneous MEG activity in brain networks. *Proc. Natl. Acad. Sci. USA* **107**, 6040–6045 (2010).
14. Leopold, D.A., Murayama, Y. & Logothetis, N.K. Very slow activity fluctuations in monkey visual cortex: implications for functional brain imaging. *Cereb. Cortex* **13**, 422–433 (2003).
15. Werner, G. & Mountcastle, V.B. The variability of central neural activity in a sensory system, and its implications for the central reflection of sensory events. *J. Neurophysiol.* **26**, 958–977 (1963).
16. Castellanos, F.X. *et al.* Varieties of attention-deficit/hyperactivity disorder-related intra-individual variability. *Biol. Psychiatry* **57**, 1416–1423 (2005).
17. Leth-Steensen, C., Elbaz, Z.K. & Douglas, V.I. Mean response times, variability, and skew in the responding of ADHD children: a response time distributional approach. *Acta Psychol. (Amst.)* **104**, 167–190 (2000).
18. Smit, D.J., Linkenkaer-Hansen, K. & de Geus, E.J. Long-range temporal correlations in resting-state  $\alpha$  oscillations predict human timing-error dynamics. *J. Neurosci.* **33**, 11212–11220 (2013).
19. Ding, N. & Simon, J.Z. Emergence of neural encoding of auditory objects while listening to competing speakers. *Proc. Natl. Acad. Sci. USA* **109**, 11854–11859 (2012).
20. Lakatos, P. *et al.* The spectrotemporal filter mechanism of auditory selective attention. *Neuron* **77**, 750–761 (2013).
21. Zion Golumbic, E.M. *et al.* Mechanisms underlying selective neuronal tracking of attended speech at a “cocktail party”. *Neuron* **77**, 980–991 (2013).
22. Freeman, J.A. & Nicholson, C. Experimental optimization of current source-density technique for anuran cerebellum. *J. Neurophysiol.* **38**, 369–382 (1975).
23. O'Connell, M.N., Barczak, A., Schroeder, C.E. & Lakatos, P. Layer specific sharpening of frequency tuning by selective attention in primary auditory cortex. *J. Neurosci.* **34**, 16496–16508 (2014).
24. O'Connell, M.N., Falchier, A., McGinnis, T., Schroeder, C.E. & Lakatos, P. Dual mechanism of neuronal ensemble inhibition in primary auditory cortex. *Neuron* **69**, 805–817 (2011).
25. Bastos, A.M. *et al.* Visual areas exert feedforward and feedback influences through distinct frequency channels. *Neuron* **85**, 390–401 (2015).
26. Buffalo, E.A., Fries, P., Landman, R., Liang, H. & Desimone, R. A backward progression of attentional effects in the ventral stream. *Proc. Natl. Acad. Sci. USA* **107**, 361–365 (2010).
27. Jensen, O. & Bonnefond, M. Prefrontal  $\alpha$ - and  $\beta$ -band oscillations are involved in rule selection. *Trends Cogn. Sci.* **17**, 10–12 (2013).
28. Michalareas, G. *et al.* Alpha-beta and gamma rhythms subserve feedback and feedforward influences among human visual cortical areas. *Neuron* **89**, 384–397 (2016).
29. Bonnefond, M. & Jensen, O. Gamma activity coupled to alpha phase as a mechanism for top-down controlled gating. *PLoS One* **10**, e0128667 (2015).
30. Spaak, E., Bonnefond, M., Maier, A., Leopold, D.A. & Jensen, O. Layer-specific entrainment of  $\gamma$ -band neural activity by the  $\alpha$  rhythm in monkey visual cortex. *Curr. Biol.* **22**, 2313–2318 (2012).
31. van Kerkoerle, T. *et al.* Alpha and gamma oscillations characterize feedback and feedforward processing in monkey visual cortex. *Proc. Natl. Acad. Sci. USA* **111**, 14332–14341 (2014).
32. Csicsvari, J., Hirase, H., Czurkó, A., Mamiya, A. & Buzsáki, G. Oscillatory coupling of hippocampal pyramidal cells and interneurons in the behaving Rat. *J. Neurosci.* **19**, 274–287 (1999).
33. McCormick, D.A., Connors, B.W., Lighthall, J.W. & Prince, D.A. Comparative electrophysiology of pyramidal and sparsely spiny stellate neurons of the neocortex. *J. Neurophysiol.* **54**, 782–806 (1985).
34. Nowak, L.G., Azouz, R., Sanchez-Vives, M.V., Gray, C.M. & McCormick, D.A. Electrophysiological classes of cat primary visual cortical neurons in vivo as revealed by quantitative analyses. *J. Neurophysiol.* **89**, 1541–1566 (2003).
35. Robbins, A.A., Fox, S.E., Holmes, G.L., Scott, R.C. & Barry, J.M. Short duration waveforms recorded extracellularly from freely moving rats are representative of axonal activity. *Front. Neural Circuits* **7**, 181 (2013).
36. Laufs, H. *et al.* Electroencephalographic signatures of attentional and cognitive default modes in spontaneous brain activity fluctuations at rest. *Proc. Natl. Acad. Sci. USA* **100**, 11053–11058 (2003).
37. Mantini, D., Perrucci, M.G., Del Gratta, C., Romani, G.L. & Corbetta, M. Electrophysiological signatures of resting state networks in the human brain. *Proc. Natl. Acad. Sci. USA* **104**, 13170–13175 (2007).
38. Murphy, K., Birn, R.M., Handwerker, D.A., Jones, T.B. & Bandettini, P.A. The impact of global signal regression on resting state correlations: are anti-correlated networks introduced? *Neuroimage* **44**, 893–905 (2009).
39. van den Brink, R.L., Wynn, S.C. & Nieuwenhuis, S. Post-error slowing as a consequence of disturbed low-frequency oscillatory phase entrainment. *J. Neurosci.* **34**, 11096–11105 (2014).
40. Haegens, S., Nacher, V., Luna, R., Romo, R. & Jensen, O.  $\alpha$ -Oscillations in the monkey sensorimotor network influence discrimination performance by rhythmic inhibition of neuronal spiking. *Proc. Natl. Acad. Sci. USA* **108**, 19377–19382 (2011).
41. Foxe, J.J. & Snyder, A.C. The role of alpha-band brain oscillations as a sensory suppression mechanism during selective attention. *Front. Psychol.* **2**, 154 (2011).
42. Saalmann, Y.B., Pinsk, M.A., Wang, L., Li, X. & Kastner, S. The pulvinar regulates information transmission between cortical areas based on attention demands. *Science* **337**, 753–756 (2012).
43. Womelsdorf, T., Valiante, T.A., Sahin, N.T., Miller, K.J. & Tiesinga, P. Dynamic circuit motifs underlying rhythmic gain control, gating and integration. *Nat. Neurosci.* **17**, 1031–1039 (2014).
44. Hutcheon, B. & Yarom, Y. Resonance, oscillation and the intrinsic frequency preferences of neurons. *Trends Neurosci.* **23**, 216–222 (2000).
45. Lakatos, P., Schroeder, C.E., Leitman, D.I. & Javitt, D.C. Predictive suppression of cortical excitability and its deficit in schizophrenia. *J. Neurosci.* **33**, 11692–11702 (2013).
46. Garrity, A.G. *et al.* Aberrant “default mode” functional connectivity in schizophrenia. *Am. J. Psychiatry* **164**, 450–457 (2007).
47. Whitfield-Gabrieli, S. *et al.* Hyperactivity and hyperconnectivity of the default network in schizophrenia and in first-degree relatives of persons with schizophrenia. *Proc. Natl. Acad. Sci. USA* **106**, 1279–1284 (2009).
48. Kim, J.S. *et al.* Power spectral aspects of the default mode network in schizophrenia: an MEG study. *BMC Neurosci.* **15**, 104 (2014).
49. Lakatos, P., O'Connell, M.N. & Barczak, A. Pondering the pulvinar. *Neuron* **89**, 5–7 (2016).
50. Calderone, D.J., Lakatos, P., Butler, P.D. & Castellanos, F.X. Entrainment of neural oscillations as a modifiable substrate of attention. *Trends Cogn. Sci.* **18**, 300–309 (2014).

## ONLINE METHODS

**Subjects.** We analyzed the electrophysiological data recorded during 36 penetrations of area A1 of the auditory cortex in 2 female rhesus macaques (ages 7 and 11 years, weighing 5–7 kg), who had been prepared surgically for chronic awake recordings. Prior to surgery, each animal was adapted to a custom fitted primate chair and to the recording chamber. All procedures were approved in advance by the Animal Care and Use Committee of the Nathan Kline Institute.

**Surgery.** Preparation of subjects for chronic awake intracortical recording was performed using aseptic techniques under general anesthesia. The tissue overlying the calvarium was resected and appropriate portions of the cranium were removed. The neocortex and overlying dura were left intact. To provide access to the brain and to promote an orderly pattern of sampling across the surface of the auditory areas, plastic recording chambers (Crist Instrument Co.) were positioned normal to the cortical surface of the superior temporal plane for orthogonal penetration of area A1, as determined by preimplant MRI. Together with socketed Plexiglas bars (to permit painless head restraint), they were secured to the skull with orthopedic screws and embedded in dental acrylic. A recovery time of 6 weeks was allowed before behavioral training and data collection began.

**Electrophysiology.** During the experiments, animals were monitored with infrared and/or low light cameras as they sat in primate chairs in a dark, isolated, electrically shielded, sound-attenuated chamber with heads fixed in position. Neuroelectric activity was obtained using linear array multicontact electrodes (23 contacts, 100- $\mu$ m intercontact spacing, Plexon Inc.). The multielectrodes were inserted acutely through guide tube grid inserts, lowered through the dura into the brain and positioned such that the electrode channels would span all layers of the cortex (Fig. 2a). Final position was determined by inspecting the laminar response profile to binaural broadband noise bursts. Neuroelectric signals were impedance-matched with a preamplifier situated on the electrode (10 $\times$  gain, bandpass DC–10 kHz), and after further amplification (500 $\times$ ) signals were recorded continuously with a 0.1–8,000 Hz bandpass digitizer with a sampling rate of 20 kHz and precision of 16 bits, using custom-written software in Labview. The signal was divided into field potential (0.1–300 Hz) and MUA (300–5,000 Hz) ranges by zero-phase-shift digital filtering (2nd-order Butterworth filter). MUA data was also rectified to improve the estimation of firing of the local neuronal ensemble<sup>51</sup>. One-dimensional current source density (CSD) profiles were calculated from the local field potential profiles using a three-point formula for the calculation of the second spatial derivative of voltage<sup>22,52</sup>. The advantage of CSD profiles is that they are not affected by volume conduction like the local field potentials, and they also provide a more direct index of the location, direction, and density of the net transmembrane current flow<sup>22,52</sup>. At the beginning of each experimental session, after refining the electrode position in the neocortex, we established the best frequency (BF) of the recording site using a ‘suprathreshold’ method<sup>53,54</sup>. This method entails presentation of a stimulus train consisting of 100 pseudorandom-order occurrences of a broadband noise burst and pure tone stimuli with frequencies ranging from 353.5 Hz to 32 kHz in half octave steps (duration: 100 ms, r/f time: 5 ms, stimulus onset asynchrony (SOA) = 624.5). Auditory stimuli were produced using Tucker Davis Technology’s System III coupled with MF-1 free field speakers.

**Behavioral task and stimuli.** We trained 2 monkeys to perform an intermodal selective attention oddball task, which required them to attend to and discriminate stimuli in one modality while ignoring stimuli in the other modality (Fig. 1). Auditory and visual stimulus streams were presented simultaneously with differing SOAs so that visual and auditory stimuli did not have a constant temporal relationship. This was meant to eliminate any multisensory binding effects and facilitate the segregation of the two different modality streams. Monkeys were cued to either detect frequency deviants occurring at random time intervals in the auditory stream, or to detect a color or intensity change in rhythmic light flashes. The auditory stream consisted of pure tone beeps at 40 dB SPL (25 ms duration, 5 ms rise/fall time) with a SOA of 624.5 ms, equivalent to a 1.6 Hz repetition rate, while the visual stream had a 1.8 Hz repetition rate. The repetition rates were set so that they would correspond to the delta frequency range of ongoing neuronal activity. The frequency of the auditory standards was parametrically varied across blocks in half octave steps between 0.3 and 32 kHz, resulting in 14 different frequency tone streams. Trial blocks using the different frequency

tone streams were presented in random order. Frequency deviants (~4 semitones different from the standard) occurred in the stream of standard tones randomly every 3–9 s. As described above, during the course of an experiment, monkeys were presented with 14 different frequency tone streams in both attend-auditory and attend-visual trial blocks, with the purpose of estimating attention-related changes in frequency tuning<sup>23</sup>. In the present study we only analyzed neuronal activity related to one of these streams for each attention condition. To avoid large-amplitude event-related responses related to preferred frequency, or best frequency (BF) tones (Fig. 2a), that can influence both spectral phase and amplitude measures, we chose to analyze non-BF trial blocks in which the tone frequency was at least 2 octaves different from the BF<sup>24</sup>. The reason for this is that although entrainment occurs, responses to non-BF tones are subthreshold in nature, without significant stimulus related MUA or CSD amplitude increases (evoked response), that could distort phase/ITC estimates<sup>20,24</sup>. We verified that there were no evoked responses related to auditory stimuli by statistically comparing the analytic (Hilbert) amplitude of pre-stimulus (–150 to –50 ms) and post-stimulus (0–100 ms) CSD averaged across all channels (Wilcoxon signed-rank tests, number of auditory trials = 299–382, all  $P > 0.05$ ). Since we wanted to calculate continuous long-timescale measures of oscillatory entrainment and dynamics, if movement-related or behavioral-response-related artifacts were obvious in the continuous recording or continuous spectrogram, we chose the trial block with the next closest frequency tone devoid of artifacts. We did originally consider including more non-BF trial blocks per experiment, but many of these had movement artifacts that would have impacted our moving alpha/ITC measures. Thus, ultimately we decided to limit our analyses to the single “cleanest” recording per attention condition.

Training of subjects on the intermodal selective attention task began with the auditory paradigm, using a single stream of tones. To facilitate the monkey’s attention to the rhythmic stimulus streams, at the start of training, 0.25–1 ml juice rewards were delivered simultaneously with each deviant through a spout. The spout was positioned such that the monkeys had to stick out their tongue to get the juice. Licking was monitored using a simple contact detector circuit<sup>55</sup>, the output of which was continuously recorded with Labview together with the timing of standard and deviant tones for offline analyses. In this early phase of training, the frequency difference between the standard and deviant tones was 1 octave. After 2 sessions, the juice reward was omitted on every 10th deviant. If the monkeys licked on the deviants without a paired juice reward, this signaled that they were attending to the tones and actively discriminating the deviants. We then omitted the reward on 20% of the deviants, and gradually lowered the frequency difference to 2–4 semitones. After 10–20 sessions on average, the monkeys’ performance became relatively stable: they were reliably licking on juiceless deviants before the next stimulus occurred in the train. At this time, we introduced the visual stream first in isolation, and after 2–3 sessions, when the monkeys reliably responded to visual deviants, we started to overlap streams. Finally, we introduced cueing streams: the same stimulus sequences used in the overlapped, intermodal selective attention blocks, but presented in one modality only to indicate the target modality for attention in the upcoming intermodal selective attention trial block. As determined by licking behavior on juiceless deviants (Fig. 1), one of the subjects performed this task correctly 76% of the time while the other monkey performed correctly only 64% of the time. Performances remained stable throughout the course of all experiments. Data collection and analysis were not performed blind to the conditions of the experiments. All experiments were performed during the day, between 8 a.m. and 5 p.m.

**Data analysis.** Data were analyzed offline using native and custom-written functions in Matlab (Mathworks, Natick, MA). After selective averaging of the CSD and MUA responses to the tones presented in the suprathreshold tonotopy paradigm, recording sites were functionally defined as belonging to A1 or belt auditory cortices based on the sharpness of frequency tuning and inspection of the tonotopic progression across adjacent sites<sup>53,56,57</sup>. Only recordings obtained from area A1 were analyzed. At the end of each animal’s experimental participation, functional assignment of the recording sites was confirmed histologically.

While we used the BF-tone related laminar CSD profiles to functionally identify cortical layers in area A1 (Fig. 2a), all further analyses were conducted on recordings during trial blocks consisting of non-BF tones (see above).

Continuous oscillatory amplitudes and phases were extracted by wavelet decomposition (Morlet wavelet,  $\sigma = 6$ ). To characterize phase distributions across

trials, the wavelet-transformed single-trial data were normalized (unit vectors), the trials were averaged and the length (modulus) of the resulting vector was computed (for example, ref. 23). The value of the mean resultant length, also called intertrial coherence (ITC), ranges from 0 to 1, with higher values indicating that the observations (oscillatory phase at a given time point across trials) are clustered more closely around the mean than lower values (i.e., phase distribution is biased). Significant deviation from uniform (random) phase distribution was tested with Rayleigh's uniformity test.

To obtain an estimate of the strength of entrainment during an entire trial block, we calculated delta ITC at the frequencies corresponding to the repetition rate of auditory (1.6 Hz) and visual stimuli (1.8 Hz) in 5-s time windows (Figs. 2b and 3a). This yielded 8 auditory and 9 visual stimulus onsets and thus phase values per window. The choice for the length of the window for moving ITC and moving alpha amplitude analyses was the result of trying to achieve a balance between number of trials for ITC measure (greater number gives a better estimate), and keeping it shorter than the average intertarget interval (6 s), so that we could capture task-structure-related fluctuations in entrainment. To achieve a relatively good frequency resolution, in the <0.2-Hz frequency range we decided to use 1-s window stepping, which resulted in a 4-s overlap. Using the Rayleigh statistic, we determined whether the ITC value for a given 5-s window was significant or not. This enabled us to sort trials into four different entrainment based categories: (i) significant delta ITC related to auditory stimuli (ITCa), (ii) significant delta ITC related to visual stimuli (ITCv), (iii) lack of any significant ITC (noITC) or (iv) ITC to both stimuli (ITCboth). Since the latter category occurred very rarely (Fig. 3b) and not in all experiments, we did not analyze neuronal activity during these time windows. Moving alpha amplitudes were calculated in the same time windows and were averaged across all cortical layers (Fig. 4a).

Given the lack of evoked responses to non-BF auditory and visual stimuli that could result in spurious phase bias, if delta ITC was significant in any given 5 s window, this indicated that delta oscillations in that period were well aligned to the timing of stimuli (Fig. 2b). Because in theory phase alignment can be incidental if the frequency of ongoing delta oscillation is similar to the repetition rate of stimuli, we also tested whether mean phases for significant ITC time periods were biased. The rationale is that if phase alignment is incidental from time to time (resulting in occasional high ITCs), this should yield a random mean phase distribution, while true entrainment should result in a biased phase distribution (i.e., similar mean phases for high ITC time periods). We found that the distributions of mean phases for significant ITC periods were significantly biased in all recordings analyzed (Rayleigh test, all  $P < 0.05$ ), for both the auditory and visual stimulus streams, indicating that significant ITC values do index oscillatory entrainment.

To compensate for the varying numbers of trials across entrainment categories potentially biasing ITC measures<sup>58</sup>, we used a repetitive combination technique to calculate ITC: for each group of trials in each experiment, we randomly drew 50 from all available trials, calculated ITC, repeated this 100 times and averaged the 100 ITC values (Fig. 3c). Burst-CSD and spike-CSD coherence values were calculated the same way. This allowed us to statistically compare delta–theta versus alpha–beta spike-CSD coherence between the groups of 100 ITC spectra for entrainment versus 100 ITC spectra for no-entrainment time periods for each single unit individually (Wilcoxon signed-rank tests,  $P < 0.01$ ; Fig. 6d).

Laminar oscillatory amplitudes were aligned across different recordings by interpolating amplitude values across channels from the electrode on the top of the cortex to the electrode on the bottom of the cortex to a constant 500 data points. This allowed us to statistically compare layer-specific amplitude changes between different entrainment conditions across all A1 recordings (Fig. 3d).

Gamma bursts were identified by first using a publicly available Matlab peak detection algorithm (peakfinder by Nathanael C. Yoder, Matlab central), using the default settings. Next, we selected bursts that had a clear peak in not just time

but also in the gamma frequency range (30–55 Hz). This was done by omitting bursts which had their largest energy peak around the “edges” of the gamma band (either at 30 or 55 Hz), to avoid wide band, usually 1/f spectral composition artifacts that would also create gamma peaks in the time domain.

Single-unit isolation and sorting was performed offline using the Plexon Offline Sorter. To avoid classifying the same units as different in attend-auditory versus attend-visual trial blocks of the same experiment due to possible electrode movement between the times when the two blocks were recorded, we only used attend-auditory trial blocks for single-unit analyses. Spike detection threshold was set manually to 3.5 s.d. of the 300- to 5,000-Hz bandpass-filtered signal. Spikes were sorted using the *K*-means algorithm, and only neurons with a downward voltage deflection followed by an upward peak were included in the analyses (Fig. 6a).

Delta and alpha coherence between all electrode pairs that yielded the laminar coherence matrices in Figure 7 were calculated at 1.6 Hz and 11 Hz using standard techniques in 5-s sliding windows, similar to those used for moving delta ITC. This allowed us to test changes in cross-laminar coherence during periods of entrainment versus no entrainment within each recording (Fig. 7a).

**Statistics.** Statistical analyses were performed in Matlab. We used either two-sided non-parametric Wilcoxon rank-sum tests or Wilcoxon signed-rank tests to compare two groups of values. To determine whether a group of values was significantly different from 0, we used a two-sided *t*-test (Fig. 7b). For multiple groups, we used either a two-way ANOVA or a Kruskal-Wallis test followed by the multiple comparison test (multcompare), using Tukey's honest significant criterion (Tukey's test). Data distribution was assumed to be normal, but this was not formally tested. Significant deviation from uniform (random) phase distribution was tested with Rayleigh's uniformity test. No statistical methods were used to predetermine sample sizes; the number of animals was minimized to conform to ethical guidelines while keeping sample sizes similar to those reported in previous publications<sup>6–8,14,24,25,30,45,59,60</sup>. No animals or data points were excluded from the analyses.

**Data availability.** The data that support the findings of this study are available from the corresponding author upon reasonable request.

A **Supplementary Methods Checklist** is available.

- Legatt, A.D., Arezzo, J. & Vaughan, H.G. Jr. Averaged multiple unit activity as an estimate of phasic changes in local neuronal activity: effects of volume-conducted potentials. *J. Neurosci. Methods* **2**, 203–217 (1980).
- Mitzdorf, U. Current source-density method and application in cat cerebral cortex: investigation of evoked potentials and EEG phenomena. *Physiol. Rev.* **65**, 37–100 (1985).
- Lakatos, P. *et al.* Timing of pure tone and noise-evoked responses in macaque auditory cortex. *Neuroreport* **16**, 933–937 (2005).
- Steinschneider, M., Reser, D., Schroeder, C.E. & Arezzo, J.C. Tonotopic organization of responses reflecting stop consonant place of articulation in primary auditory cortex (A1) of the monkey. *Brain Res.* **674**, 147–152 (1995).
- Slotnick, B. A simple 2-transistor touch or lick detector circuit. *J. Exp. Anal. Behav.* **91**, 253–255 (2009).
- Merzenich, M.M. & Brugge, J.F. Representation of the cochlear partition of the superior temporal plane of the macaque monkey. *Brain Res.* **50**, 275–296 (1973).
- Rauschecker, J.P., Tian, B., Pons, T. & Mishkin, M. Serial and parallel processing in rhesus monkey auditory cortex. *J. Comp. Neurol.* **382**, 89–103 (1997).
- Maris, E., Schoffelen, J.M. & Fries, P. Nonparametric statistical testing of coherence differences. *J. Neurosci. Methods* **163**, 161–175 (2007).
- Kajikawa, Y., Falchier, A., Musacchia, G., Lakatos, P. & Schroeder, C.E. in *The Neural Bases of Multisensory Processes* (eds. Murray, M.M. & Wallace, M.T.) 65–98 (CRC Press, 2012).
- Schroeder, C.E., Molholm, S., Lakatos, P., Ritter, W. & Foxe, J.J. Human–simian correspondence in the early cortical processing of multisensory cues. *Cogn. Process.* **5**, 140–151 (2004).